

Enhanced Superconductivity in Bilayer PtTe₂ by Alkali-Metal Intercalations

Danhong Wu,¹ Yiping Lin,¹ Lingxiao Xiong,¹ Junjie Li,¹ Tiantian Luo,¹ Deyi Chen,¹ and Feipeng Zheng^{1,*}

¹*Siyuan Laboratory, Guangzhou Key Laboratory of Vacuum Coating Technologies and New Energy Materials, Department of Physics, Jinan University, Guangzhou 510632, China*

Layered platinum tellurium (PtTe₂) were recently synthesized with controllable layer numbers down to monolayer limit. Using *ab initio* calculation based on anisotropic Migdal-Eliashberg formalism, we show that by rubidium (Rb) intercalation, weak superconductivity in bilayer PtTe₂ can be significantly boosted with superconducting $T_c = 8$ K in the presence of spin-orbit coupling (SOC). The intercalant on one hand mediates the interlayer coupling and serve as an electron donor, leading to large density of states at Fermi energy. On the other hand, it increases the mass-enhancement parameter with electron-phonon coupling strength comparable to that of Pt. The potassium intercalated bilayer PtTe₂ has a comparable T_c to the case of Rb intercalation. The relatively high T_c with SOC combined with experimental accessible crystal structures suggest that these superconductors are promising platforms to study the novel quantum physics associated with two-dimensional superconductivity, such as the recently proposed type-II Ising superconductivity.

I. INTRODUCTION

Transition metal dichalcogenides (TMDCs) exhibit intriguing physical properties including superconductivity, charge-density wave, Dirac semimetals, among which the two-dimensional (2D) superconductivity has received growing attention, where the reduced dimensionality leads to unique behaviors compared to their bulk counterparts. One notable example is monolayer NbSe₂: (1) the enhanced charge-density wave and reduced superconductivity in going from bulk to the monolayer [1]; (2) the transition from a two-gap superconductor (bulk) to a single-gap one (monolayer) [2, 3], owing to the competition between charge-density wave and superconductivity [4]; (3) suppressed magnetic instability by charge-density wave [5]; (4) Ising superconductivity, where the inversion-symmetry-broken crystal leads to large Zeeman type spin-orbit coupling (SOC), resulting in the extremely large in-plane upper critical field [6, 7]. Besides the inversion-symmetry-broken Ising superconductivity, the large critical fields were also observed in 2D centrosymmetric systems known as type-II Ising superconductivity, arising from multiple degenerate orbitals with spin-orbital locking [8–10]. Clearly, realizing 2D superconductivity in layered TMDCs is desirable to offer potential platforms for studying the novel quantum physics and the interplay among different orders in 2D limit.

The group VIII TMDCs, MTe₂, where M=Ni, Pd, Pt, recently attract increasing attentions for the experimentally verified type-II Dirac semimetal [11–13], pressure induced superconductivity in their bulk phases [14, 15], and novel physics in their ultrathin films [9, 16–21]. In particular, monolayer NiTe₂ was predicted to be an intrinsic superconductor, and lithium intercalation can boost the superconducting transition temperature (henceforth T_c) of bilayer NiTe₂ up to 11.3 K [16]. Few-layer PdTe₂ were experimentally verified to be type-II Ising superconductors though with $T_c < 1$ K [21]. Very recently, their homologues PtTe₂ crystals were reported to be synthesized

with controllable thickness down to monolayer limit [18]. Different from NiTe₂, monolayer PtTe₂ is an intrinsic semiconductor with band gap about 0.8 eV. Interlayer coupling in PtTe₂ is expected to be stronger, due to the smaller interlayer spacing in bulk PtTe₂. Furthermore, SOC is supposed to be stronger in PtTe₂, as Pt element is much heavier than Pd and Ni. The above differences, combined with the longing for the 2D superconductor motivate us to study the possibility of the emergence of superconductivity in 2D PtTe₂ crystals.

This Letter reports an *ab initio* study on electron-phonon coupling (EPC) and superconducting properties of PtTe₂. We show that the weak superconductivity in bilayer PtTe₂ (Pt₂Te₄) can be significantly boosted by alkali-metal intercalations. In particular, rubidium (Rb) intercalation leads to the formation of a thermodynamically stable crystal with the stoichiometry of RbPt₂Te₄, where the Rb occupy all the octahedral sites. Based on anisotropic Migdal-Eliashberg formalism, the T_c of the RbPt₂Te₄ is computed to be 8 K with SOC, which is very high among TMDCs. The homologues KPt₂Te₄ is shown to have comparable T_c to RbPt₂Te₄. The mechanism of the remarkable boosted superconductivity and the effect of SOC are systematically analyzed.

II. COMPUTATIONAL METHODS

Density-functional theory and density-functional perturbation theory calculations were performed with the exchange-correlation functional of PBE [22] to study the crystal structures, electronic structures, EPC of bulk, and few-layer PtTe₂ before and after alkali-metal intercalations [23, 24]. The norm-conserving pseudopotentials of FHI98 [25] and ONCV [26] were used to describe the interaction between valence and core electrons. The Kohn-shame valence states were expanded as plane waves below 80 Rydberg. A 18×18 ($18 \times 18 \times 12$) \mathbf{k} -mesh and a 6×6 ($6 \times 6 \times 4$) \mathbf{q} -mesh were adopted to cal-

culate the ground states of charge density and phonons for few-layer (bulk) systems, whereupon the electron-phonon coupling (EPC) matrix element $g_{mn,\nu}(\mathbf{k}, \mathbf{q})$ are calculated, which quantifies the scattering amplitude between the electronic states with wavevector \mathbf{k} , band index m (\mathbf{k}, m), and ($\mathbf{k}+\mathbf{q}, n$) via a phonon with branch ν and wavevector \mathbf{q} . Then above quantities are interpolated to the \mathbf{k} -grid of 120×120 ($60 \times 60 \times 36$) and \mathbf{q} -grid of 60×60 ($30 \times 30 \times 20$) [27, 28], based on which the mass-enhancement parameter $[\alpha^2 F(\omega)/\omega]$ are computed, where $\alpha^2 F(\omega)$ is the Eliashberg spectrum, defined as:

$$\alpha^2 F(\omega) = \frac{1}{2} \sum_{\nu} \int_{\text{BZ}} \frac{d\mathbf{q}}{\Omega_{\text{BZ}}} \omega_{\mathbf{q}\nu} \lambda_{\mathbf{q}\nu} \delta(\omega - \omega_{\mathbf{q}\nu}), \quad (1)$$

where $\lambda_{\mathbf{q}\nu}$ are phonon-momentum-resolved EPC constant [27], Ω_{BZ} is the volume of the 1st Brillouin zone, and $\delta(\omega - \omega_{\mathbf{q}\nu})$ is replaced with a gaussian function with a broadening of 0.5 meV. Using the same \mathbf{k} - and \mathbf{q} -grids, the temperature-dependent superconducting gaps $[\Delta(\mathbf{k}, T)]$ are obtained by solving the anisotropic Migdal-Eliashberg equations with the Matsubara frequencies below 0.23 eV on imaginary axis [27, 29], followed by performing analytic continuation to the real axis with Padé functions.

III. RESULTS AND DISCUSSIONS

Monolayer PtTe₂ is composed of Te-Pt-Te triatomic layers, where each Pt is octahedral-coordinated by six Te atoms. Its bulk counterpart, 1T-PtTe₂ is formed by the AA stacking of such monolayers along z direction, separated by an interlayer spacing $d = 2.57 \text{ \AA}$ [30], with the hexagonal lattice constants $a = 4.01$ and $c = 5.24 \text{ \AA}$ [18]. The optimized lattice constants are $a = 4.08$, and $c = 5.27 \text{ \AA}$ using the FHI98 pseudopotential [25], in nice agreement with the experiment. To study the SOC effect on EPC and superconducting properties, we also adopt the ONCV pseudopotential [26], which yields the optimized $a = 4.10$, and $c = 5.38 \text{ \AA}$, slightly larger the experimental one. Nonetheless, we found that the above two pseudopotentials yield consistent computational results (see Sec. S1 [31] for details). In addition to the different pseudopotentials, the van der Waals (vdW) correlations [32–34] are also found to have little influence on the electronic structures (see Sec. S1[31]). Therefore, we mainly report in the main text, the results of the ONCV without vdW correction. It should also be mentioned that we involve the projector augmented wave type of pseudopotentials for more efficient calculations of *ab initio* molecular dynamic (AIMD), and the determination of convex hull for the Rb intercalated bilayer PtTe₂, which will be discussed soon. More details of the motivation of using the above methods can be found [35]. The interlayer distance $d = 2.57 \text{ \AA}$ of the bulk PtTe₂ is

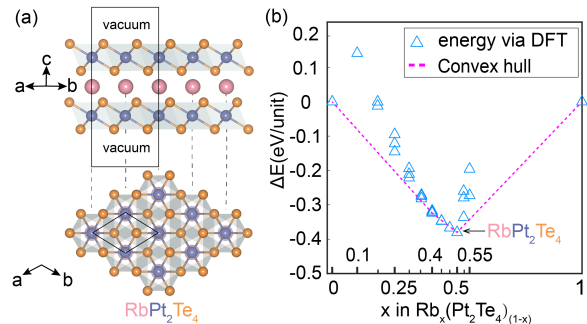


FIG. 1. (a) Side and top views of a slab model of rubidium intercalated bilayer PtTe₂ (schematic diagram). The black rhombus indicates a two-dimensional hexagonal unit cell. (b) Formation energies as a function of Rb concentration (x) calculated in a 3×3 supercell via density-functional theory (DFT; see main text). The dashed pink line illustrates the convex hull between bilayer PtTe₂ ($x = 0$) and the body-centered cubic rubidium crystal ($x = 1$).

much smaller than that of other layered TMDCs (e.g., 2.90 \AA for 2H-NbSe₂ [36], 2.89 \AA for T_d-WTe₂ [37]) and even smaller than its homologues NiTe₂ (2.63 \AA) [38], indicating the potential strong interlayer coupling. Indeed, it was reported that the dispersive bandstructure along c^* suppresses its superconductivity in bulk PtTe₂ [39]. Besides, our computational results show that the electron-doped monolayer PtTe₂ can exhibit overall large EPC strength (λ) and isotropic superconducting T_c as shown in Sec. S2 [31]. Therefore, it is expected that the superconductivity can be emerged in PtTe₂ by electron doping and weakening the interlayer coupling. Thus, to enhance the superconductivity in layered PtTe₂, the intercalation of alkali-metal atoms should be a reasonable way, as the intercalants can act as electron donors and relieve the interlayer coupling by expanding the interlayer spacing. To realize 2D superconductivity in PtTe₂, we then study the alkali-metal intercalated bilayer PtTe₂.

We begin by studying the energy favorable geometry structures of Rb-intercalated bilayer PtTe₂, whose stoichiometry can be generated as Rb _{m} (Pt₂Te₄) _{n} , where m and n are integers, counting the number of Rb and Pt₂Te₄ units, respectively. We use a 3×3 supercell to calculate the formation energies ΔE with respect to the Rb concentration fraction $x = m/(m + n)$, defined as $\Delta E(x) = E[\text{Rb}_x(\text{Pt}_2\text{Te}_4)_{1-x}] - x E[\text{Rb}] - (1-x) E[\text{Pt}_2\text{Te}_4]$, where $E[\text{Rb}]$ and $E[\text{Pt}_2\text{Te}_4]$ are the energies of a body-center cubic Rb crystal per atom and a bilayer PtTe₂ per Pt₂Te₄ unit, respectively. Fig. 1(b) displays the corresponding results, where $\Delta E(x)$ decrease as the increase of x and reach the minimum at $x = 0.5$, corresponding to the crystal with the stoichiometry RbPt₂Te₄. Further increasing the number of Rb, the ΔE begins to increase. The resultant convex hull shown in Fig. 1(b) suggests that the RbPt₂Te₄ crystal is thermodynamically stable with respect to any other stoichiometry. Fig. 1(a)

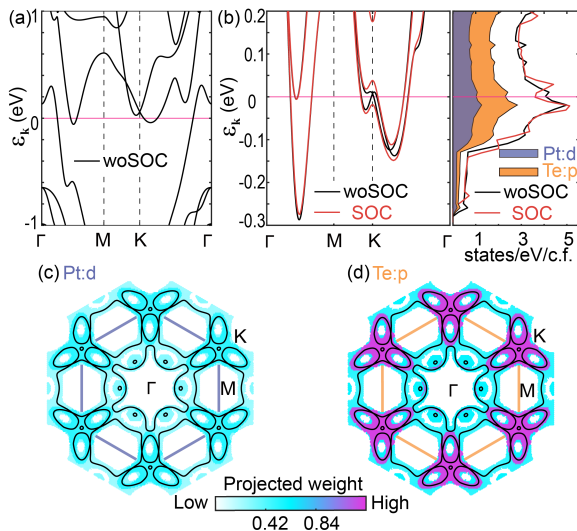


FIG. 2. (a) Electronic bandstructure of bilayer PtTe_2 . (b) Electronic bandstructures of RbPt_2Te_4 with/without SOC. The corresponding projected DOS (without SOC) onto p -like orbitals of Te and d -like orbitals of Pt atoms are shown in the right panel. The projected weights (without SOC) onto the d -like orbitals (c) and p -like orbitals (d) for the electronic states of RbPt_2Te_4 within an energy window of 100 meV near ϵ_F . The colors of the dots represent the projection weights (see the colorbar). The black solid lines indicate the Fermi surface and the hexagons are the first Brillouin zone.

displays the crystal structure of the RbPt_2Te_4 , where the Rb atoms occupy all the octahedral sites at the mid-points of the nearest pairs of Pt atoms in the adjacent monolayers, which is similar to the case of lithium intercalated bilayer NiTe_2 [16]. AIMD simulations [24, 40] further suggest that the RbPt_2Te_4 crystal is stable at room temperature without structure distortion in 10 picoseconds (see Sec. S3 [31]).

Figs. 2(a) and S4(a) display the electronic bandstructures of bilayer (henceforth Pt_2Te_4) and monolayer PtTe_2 , respectively. The monolayer is computed to have a band gap of 0.8 eV, which agrees well with the experiment [18]. On going from the monolayer to the bilayer, a semiconductor-to-metal transition is seen with the strong modification of the electronic structure around Fermi energy (ϵ_F). The mostly remarkable change is a band derived mainly from the p_z -like orbitals of Te drops down and crosses ϵ_F (see Sec. S4 for the projected bandstructures [31]). This can be assigned to the overlap between the p_z -like orbitals of the Te atoms in the bilayer, suggesting the strong interlayer coupling. The calculated bandstructure of the Pt_2Te_4 is again consistent with the ARPES measurements [18]. After Rb intercalation, the interlayer spacing expands and the interlayer coupling weakens, accompanied by the electrons transfer from Rb to its adjacent Te layers. The synergy effects of Rb-mediated interlayer coupling and electron doping make the bandstructure of the RbPt_2Te_4 resemble that of the

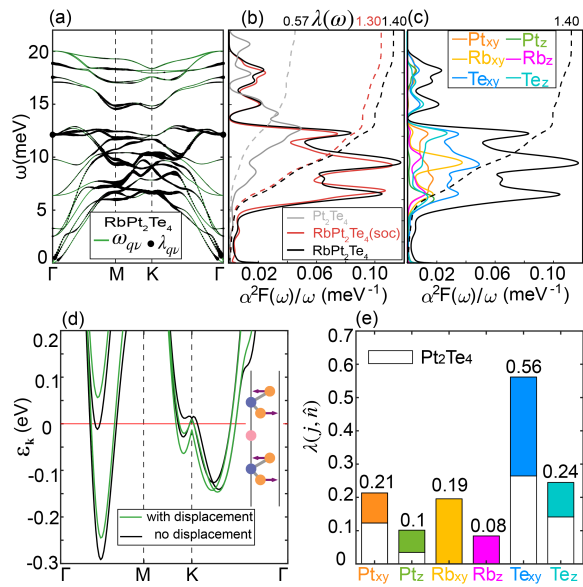


FIG. 3. (a) Phonon dispersion ($\omega_{q\nu}$) of RbPt_2Te_4 without SOC, and its corresponding EPC constants $\lambda_{q\nu}$. (b) The mass-enhancement parameters $\alpha^2 F(\omega)/\omega$ of Pt_2Te_4 and RbPt_2Te_4 with/without SOC. (c) Partial mass-enhancement parameters $\alpha^2 F(\omega, j, \hat{n})/\omega$, where $j = \text{Pt, Te, Rb}$, and \hat{n} is the unit projection direction vector. (d) Bandstructures of RbPt_2Te_4 (without SOC) with/without atomic displacements of the phonon modes shown in the inset (see main text). The displacements are tabulated in Table S2 [31], where one can see the Te atoms have the largest displacements of about 0.05 Å. (e) Partial EPC constants arising from various atomic vibrations: $\lambda(j, \hat{n}) = 2 \int_0^\infty d\omega \alpha^2 F(\omega, j, \hat{n})/\omega$.

electron doped monolayer PtTe_2 , but with slight band splitting [compare Figs. 2(b) and S4(a)]. One can see from Fig. 2(b) that without SOC, there are two conduction bands crossing the ϵ_F , leading to the formation of several electron pockets depicted by the solid black circles in Figs. 2(c)–2(d). The two bands intersect at the Brillouin zone corners, K and K', at the energy ~ 12 meV above ϵ_F , which is responsible for the emergent tiny circles centered at K and K'. When the SOC is included, though the Kramers degeneracy is preserved due to the inversion symmetry at the site of Rb, the double degenerated bands at K and K' are split, leading to the avoided crossing near ϵ_F and a ~ 57 meV gap opening at K and K', giving rise to a slight reduced density of states at ϵ_F [$N(0)$]. In addition to the small Fermi circles, the clover-shaped pockets centered at K and K' are also noted, each of them consists of three separate petals. Centered at M and Γ points, there are also two electron pockets. The calculated projected electronic density of states (DOS) [right panel of Fig. 2(b)] and the momentum-resolved DOS for the states near ϵ_F [Figs. 2(c)–2(d)] suggest that these states near K, K' are significantly contributed by the p -like orbitals, and the remaining states are assigned to the hybridization of the d - and p -like orbitals.

The computed phonon dispersions ($\omega_{\mathbf{q}\nu}$) of the RbPt₂Te₄ [Figs. 3(a) and S5(b)] and Pt₂Te₄ [Fig. S5(a)] show that all the $\omega_{\mathbf{q}\nu} \geq 0$, suggesting the dynamical stabilities of the crystals. The SOC is found to have little influence on $\omega_{\mathbf{q}\nu}$ of RbPt₂Te₄ [Fig. S5(b)], and slightly decrease the intensity of the mass-enhancement parameter [$\alpha^2 F(\omega)/\omega$; see Fig. 3(b)], but the main features of the $\alpha^2 F(\omega)/\omega$ is similar to the case without SOC. For easier analysis, we first focus on the case without SOC. Fig. 3(b) displays the comparison of the $\alpha^2 F(\omega)/\omega$ and the corresponding accumulated EPC strength $\lambda(\omega) = 2 \int_0^\omega \alpha^2 F(\omega')/\omega' d\omega'$ (dashed lines) between RbPt₂Te₄ and Pt₂Te₄. It is found that after the intercalation of Rb, the $\lambda(\omega)$ are remarkably enhanced in the energy region between 5 – 13 meV. Particularly, three intensive peaks are found located at 6.6, 9.6 and 12.3 meV, respectively. To further study the mechanism of the enhanced EPC, we decomposed the $\alpha^2 F(\omega)$ into the contributions from in-plane (xy) and out-of-plane (z) vibrations of each atom by computing

$$\alpha^2 F(\omega, j, \hat{n}) = \frac{1}{2} \sum_{\nu} \int_{\text{BZ}} \frac{d\mathbf{q}}{\Omega_{\text{BZ}}} \omega_{\mathbf{q}\nu} \lambda_{\mathbf{q}\nu} \delta(\omega - \omega_{\mathbf{q}\nu}) |\hat{n} \cdot \mathbf{e}_{\mathbf{q},\nu}^j|^2, \quad (2)$$

where $\mathbf{e}_{\mathbf{q},\nu}^j$ is the component of atom j (Pt, Rb, Te) in the eigenvector of the dynamic matrix with phonon momentum \mathbf{q} and modes ν , and \hat{n} is the unit projection direction vector, which is chosen along in-plane (xy) and out-of-plane (z) directions. The computed $\alpha^2 F(\omega, j, \hat{n})/\omega$ and the corresponding accumulated EPC constants $\lambda(j, \hat{n}) = 2 \int_0^\omega d\omega' \alpha^2 F(\omega', j, \hat{n})/\omega'$ are shown in Figs. 3(c) and 3(e), respectively. The most remarkable change is the doubled $\lambda(\text{Te}_{xy})$ to 0.56 after the Rb intercalation [Fig. 3(e)]. This is consistent with the computed $\alpha^2 F(\omega, \text{Te}_{xy})/\omega$ [Fig. 3(c)], where $\alpha^2 F(\omega, \text{Te}_{xy})/\omega$ dominates the total spectrum of $\alpha^2 F(\omega)/\omega$ in 5 – 13 meV, suggesting the strongly coupling of the in-plane vibration of Te atoms with the electrons. In particular, the two pairs of double degenerated modes E_g and E_u can be seen at Γ with energy of 12.08 and 12.11 meV, respectively [Fig. 3(a)], which are derived from Te_{xy} vibrations [see Fig. S6(a) [31]]. Among them, the two E_g modes exhibit large $\lambda_{\mathbf{q}\nu}$. The vibrational pattern for one of the E_g is shown in the inset of Fig. 3(d). By comparing the bandstructures with and without such phonon displacements imposed on the equilibrant RbPt₂Te₄ crystal, one can see that the Te_{xy} displacements have strong influences on the bands near ϵ_F , especially around K, where a Lifshitz transition is noted [Fig. 3(d)]. The secondary contributions to λ arise from the Te_z , Pt_{xy} and Rb_{xy} vibrations as shown in Fig. 3(e). By further examining the corresponding spectra in Fig. 3(c), one can see that the contribution of Te_z vibration is mainly associated with the peaks at 6.6 and 12.3 meV, while Pt_{xy} exhibits a relatively uniform contribution in the whole energy region. Interestingly, the Rb also exhibits moderate contribution

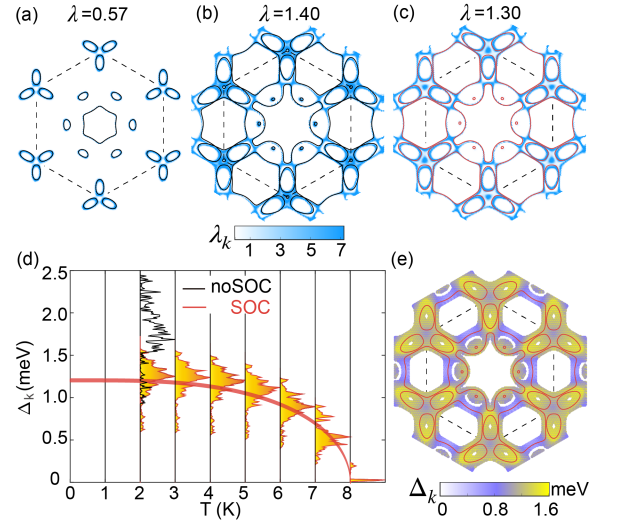


FIG. 4. Electronic momentum-resolved EPC constants $\lambda_{\mathbf{k}}$ (see main text) for Pt₂Te₄ (a), RbPt₂Te₄ without (b) and with (c) spin-orbit coupling. The corresponding Fermi surfaces are indicated by the solid lines. (d) Histograms of temperature-dependent superconducting gaps $\Delta_{\mathbf{k}}(T)$ for those electronic states \mathbf{k} , whose Kohn-Sham energies are 0.1 eV around ϵ_F . (e) The distribution of the $\Delta_{\mathbf{k}}$ at $T = 2$ K in an extensive Brillouin zone. SOC is taken into account.

to λ , as the computed $\lambda(\text{Rb}) = 0.27$ is comparable to $\lambda(\text{Pt}) = 0.31$ [see Fig. 3(e)]. The Rb vibrations promote the $\alpha^2 F(\omega)/\omega$ peak at 9.6 meV [Fig. 3(c)], being on par with the contribution of Te_{xy} at the same energy.

We turn to study the mechanism of the enhanced EPC in RbPt₂Te₄ by analyzing the electronic states involved in EPC. We computed the \mathbf{k} -resolved EPC constant $\lambda_{\mathbf{k}}$, defined as follow in this work:

$$\lambda_{\mathbf{k}} = \frac{1}{N(0)} \sum_{m,n,\nu} \int \frac{d\omega}{\omega} \int \frac{d\mathbf{q}}{\Omega_{\text{BZ}}} |g_{mn,\nu}(\mathbf{k}, \mathbf{q})|^2 \delta(\epsilon_{n\mathbf{k}}) \times \delta(\epsilon_{m\mathbf{k}+\mathbf{q}}) \delta(\omega - \omega_{\mathbf{q}\nu}), \quad (3)$$

where Ω_{BZ} is the volume of the first Brillouin zone, $g_{mn,\nu}(\mathbf{k}, \mathbf{q})$ is the EPC matrix element, and the δ functions related to electron and phonon energies are replaced by gaussian functions with broadening of 10 and 0.5 meV, respectively. The $\lambda_{\mathbf{k}}$ is related to total EPC constant by $\lambda = \int \frac{d\mathbf{k}}{\Omega_{\text{BZ}}} \lambda_{\mathbf{k}}$. By comparing $\lambda_{\mathbf{k}}$ of Pt₂Te₄ and RbPt₂Te₄ shown in Figs. 4(a) and 4(b), one can see the clover-shaped circles at K and K' are expanded, and the additional Fermi circles emerge after Rb intercalation, promoting the $N(0)$ from 1.54 to 4.09 states/eV/Pt. Consequently, the λ in RbPt₂Te₄ is remarkably boosted to 1.4, as more pairs of electronic states can be involved in the EPC. Furthermore, the contribution of the λ of RbPt₂Te₄ are almost arising from the \mathbf{k} near K and K' as shown in Fig. 4(b), which are mainly derived from the electronic states of Te atoms [Fig. 2(d)]. By similar anal-

ysis, the states in the remaining sections of the Fermi surface, derived from the p - d hybridization of Te and Pt atoms, also contribute to λ . The SOC is found to reduce the $\lambda_{\mathbf{k}}$ near K, K' [Fig. 4(c)], attributable to the reduced $N(0)$ arising from band splitting at K, K' [Fig. 2(b)]. Consequently, λ decreases to 1.3 with SOC. Except that, the main feature of the computed $\lambda_{\mathbf{k}}$ is unchanged. Therefore, it is evident that the large $\lambda_{\mathbf{k}}$ in RbPt₂Te₄ is mainly contributed by the pairing of electronic states of Te atoms near K, K' Fermi pockets.

The significantly enhanced λ indicates the boost of the superconducting T_c . Indeed, using McMillan-Allen-Dynes approach [41–43] based on the calculated $\lambda = 1.30$, the logarithmic average of the phonon frequencies $\omega_{\log} = 104.5$ K, and $\mu^* = 0.205$ evaluated by $\mu^* \approx [0.26N(0)/[1 + N(0)]]$ [44], the isotropic superconducting T_c of RbPt₂Te₄ is calculated to be 6.6 K with SOC. In contrast, the computed T_c for Pt₂Te₄ are only 1.1 K. The reliability of the computed isotropic T_c is also examined by computing bulk PtTe₂ as discussed in Sec. S7, where one can see the computed λ for bulk PtTe₂ is 0.35 and the corresponding T_c is 0 K, in nice agreement with previous study that the bulk PtTe₂ is non-superconducting with $\lambda = 0.33$ [39]. To obtain more reliable superconducting T_c for the systems with reduced dimensionality and anisotropic Fermi surface [29, 45, 46], we further evaluate the T_c of RbPt₂Te₄ by solving the full Midgal-Eliashberg gap equation [29, 45]. Compared to the slight decrease of the aforementioned isotropic λ , the SOC has relatively noticeable influences on the anisotropic superconducting properties. Fig. 4(d) shows the evolution of the energy distribution of superconducting gaps ($\Delta_{\mathbf{k}}$) with respect to temperatures. At $T = 2$ K without SOC, the $\Delta_{\mathbf{k}}$ are distributed in the energy range between 0.9 – 2.4 meV with an average value of 1.6 meV, showing strong anisotropy. When SOC is involved, the overall decreased $\Delta_{\mathbf{k}}$ and the suppressed anisotropic distribution of $\Delta_{\mathbf{k}}$ are seen, as the average value of $\Delta_{\mathbf{k}}$ decreases to ~ 1.2 meV, and the energy distribution range is reduced to 0.6 – 1.6 meV. The corresponding distribution of $\Delta_{\mathbf{k}}$ in an extended Brillouin zone is shown in Fig. 4(e), where one can see that the $\Delta_{\mathbf{k}}$ exhibit anisotropic distribution to some extents, in which the relatively large $\Delta_{\mathbf{k}}$ comes from the Fermi pockets around K and K', dominated by the electronic states of Te atoms as analyzed before. As the temperature increases, the values of $\Delta_{\mathbf{k}}$ gradually reduce and finally vanish at $T = 8$ K, suggesting the T_c of the RbPt₂Te₄ is ~ 8 K, which is higher than the isotropic one (6.6 K) due to the anisotropic $\Delta_{\mathbf{k}}$. We also study the intercalation of other alkali metal elements including lithium (Li), sodium (Na), potassium (K) and caesium (Cs), in which the KPt₂Te₄ is expected to have comparable T_c to the RbPt₂Te₄, followed by the T_c of CsPt₂Te₄, whereas the LiPt₂Te₄ and NaPt₂Te₄ are with relatively low T_c [see Sec. S8 for details].

IV. CONCLUSION

In summary, we have predicted the enhanced EPC and superconducting T_c in RbPt₂Te₄ and understood the corresponding mechanisms from *ab initio* calculations. Firstly, according to the computed convex hull, phonon dispersions and *ab initio* molecular dynamic simulations, the intercalated Rb are energetically favorable to occupy all the octahedral sites in the interlayer gallery, forming the thermodynamically stable RbPt₂Te₄ crystal. The T_c of RbPt₂Te₄ is computed to be 8 K with the anisotropic superconducting gaps based on the anisotropic Midgal-Eliashberg formalism in the presence of SOC, though the pristine Pt₂Te₄ have a very low T_c . Such a remarkable enhancement is assigned to the effects of the Rb intercalations from two sides. On one hand, the synergy effect of Rb-mediated interlayer coupling and electron doping lead to the significant promotion of $N(0)$, accompanied by the markedly enhanced EPC of Te phonons. On the other hand, the Rb directly contributes to the EPC by significantly increasing the intensity of $\alpha^2 F(\omega)/\omega$ peak at 9.6 meV. The SOC reduces the T_c and the anisotropic superconducting gaps by splitting the band degeneracy near ϵ_F . The KPt₂Te₄ is proposed to have comparable T_c to the RbPt₂Te₄. The reliability of our predictions is supported by the consistent computational results of electronic structures of few-layer PtTe₂, and the EPC and superconductivity of bulk PtTe₂ with previous studies.

Considering bilayer PtTe₂ has been experimentally synthesized [18], and the intercalation of alkali-metal atoms therein can be experimentally realized [47–50], our predictions can be straightforwardly probed. Therefore, the experimental accessibility, combined with the relatively high superconducting T_c with SOC will make these superconductors promising platforms to investigate intriguing novel quantum physics associated with 2D superconductivity. For example, as we have shown before, the RbPt₂Te₄ crystal has three-fold rotational symmetries, which are preserved at high symmetry momenta of K and K', at which the double degenerated electronic bands very close to ϵ_F are noted without SOC, and they will be further split by SOC [Fig. 2(b)]. The KPt₂Te₄ also exhibits similar results (Fig. S10). The above results suggest that the alkali-metal intercalated bilayer PtTe₂ are potential candidates for realizing the type-II Ising superconductivity with relatively high superconducting T_c [8], which calls for further studies.

This work is supported by National Natural Science Foundation of China (Grants No. 11804118), Guangdong Basic and Applied Basic Research Foundation (Grants No. 2021A1515010041), open project funding of Guangzhou Key Laboratory of Vacuum Coating Technologies and New Energy Materials (KFVEK-FVE20200001). The Calculations were performed on

high-performance computation cluster of Jinan University, and Tianhe Supercomputer System.

D.H. Wu, Y.P. Lin and L.X. Xiong contribute equally to this work.

* fpzheng_phy@email.jnu.edu.cn

- [1] X. Xi, L. Zhao, Z. Wang, H. Berger, L. Forró, J. Shan, and K. F. Mak, *Nat. Nanotechnol.* **10**, 765 (2015).
- [2] Y. Noat, J. A. Silva-Guillén, T. Cren, V. Cherkez, C. Brun, S. Pons, F. Debontridder, D. Roditchev, W. Sacks, L. Cario, P. Ordejón, A. García, and E. Canadell, *Phys. Rev. B* **92**, 134510 (2015).
- [3] E. Khestanova, J. Birkbeck, M. Zhu, Y. Cao, G. L. Yu, D. Ghazaryan, J. Yin, H. Berger, L. Forró, T. Taniguchi, K. Watanabe, R. V. Gorbachev, A. Mishchenko, A. K. Geim, and I. V. Grigorieva, *Nano Lett.* **18**, 2623 (2018),.
- [4] F. Zheng and J. Feng, *Phys. Rev. B* **99**, 161119 (2019).
- [5] F. Zheng, Z. Zhou, X. Liu, and J. Feng, *Phys. Rev. B* **97**, 081101(R) (2018).
- [6] X. Xi, Z. Wang, W. Zhao, J.-H. Park, K. T. Law, H. Berger, L. Forró, J. Shan, and K. F. Mak, *Nat. Phys.* **12**, 139 (2016),.
- [7] Y. Xing, K. Zhao, P. Shan, F. Zheng, Y. Zhang, H. Fu, Y. Liu, M. Tian, C. Xi, H. Liu, J. Feng, X. Lin, S. Ji, X. Chen, Q. K. Xue, and J. Wang, *Nano Lett.* **17**, 6802 (2017),.
- [8] C. Wang, B. Lian, X. Guo, J. Mao, Z. Zhang, D. Zhang, B. L. Gu, Y. Xu, and W. Duan, *Phys. Rev. Lett.* **123**, 126402 (2019),.
- [9] M. Liu, C. Wu, Z. Liu, Z. Wang, D. X. Yao, and D. Zhong, *Nano Res.* **13**, 1733 (2020),.
- [10] J. Falson, Y. Xu, M. Liao, Y. Zang, K. Zhu, C. Wang, Z. Zhang, H. Liu, W. Duan, K. He, H. Liu, J. H. Smet, D. Zhang, and Q. K. Xue, *Science* **367**, 1454 (2020).
- [11] K. Zhang, M. Yan, H. Zhang, H. Huang, M. Arita, Z. Sun, W. Duan, Y. Wu, and S. Zhou, *Phys. Rev. B* **96**, 125102 (2017).
- [12] M. Yan, H. Huang, K. Zhang, E. Wang, W. Yao, K. Deng, G. Wan, H. Zhang, M. Arita, and H. Yang, *Nat. Commun.* **8**, 257 (2017).
- [13] H. Huang, S. Zhou, and W. Duan, *Phys. Rev. B* **94**, 121117 (2016).
- [14] M. Qi, C. An, Y. Zhou, H. Wu, B. Zhang, C. Chen, Y. Yuan, S. Wang, Y. Zhou, X. Chen, R. Zhang, and Z. Yang, *Phys. Rev. B* **101**, 1 (2020).
- [15] R. C. Xiao, P. L. Gong, Q. S. Wu, W. J. Lu, M. J. Wei, J. Y. Li, H. Y. Lv, X. Luo, P. Tong, X. B. Zhu, and Y. P. Sun, *Phys. Rev. B* **96**, 075101 (2017).
- [16] F. Zheng, X.-B. Li, Y. Lin, L. Xiong, and J. Feng, *Phys. Rev. B* **101**, 100505(R) (2020),.
- [17] B. Zhao, W. Dang, Y. Liu, B. Li, J. Li, J. Luo, Z. Zhang, R. Wu, H. Ma, and G. Sun, *J. Am. Chem. Soc.* **140**, 14217 (2018).
- [18] M. K. Lin, R. A. B. Villaos, J. A. Hlevyack, P. Chen, R. Y. Liu, C. H. Hsu, J. Avila, S. K. Mo, F. C. Chuang, and T. C. Chiang, *Phys. Rev. Lett.* **124**, 036402 (2020).
- [19] K. Deng, M. Yan, C. P. Yu, J. Li, X. Zhou, K. Zhang, Y. Zhao, K. Miyamoto, T. Okuda, W. Duan, Y. Wu, X. Zhong, and S. Zhou, *Sci. Bull.* **64**, 1044 (2019).
- [20] C. Liu, C. S. Lian, M. H. Liao, Y. Wang, Y. Zhong, C. Ding, W. Li, C. L. Song, K. He, X. C. Ma, W. Duan, D. Zhang, Y. Xu, L. Wang, and Q. K. Xue, *Phys. Rev. Mater.* **2**, 094001 (2018).
- [21] Y. Liu, Y. Xu, J. Sun, C. Liu, Y. Liu, C. Wang, Z. Zhang, K. Gu, Y. Tang, C. Ding, H. Liu, H. Yao, X. Lin, L. Wang, Q. K. Xue, and J. Wang, *Nano Lett.* **20**, 5728 (2020).
- [22] J. P. Perdew, K. Burke, and M. Ernzerhof, *Phys. Rev. Lett.* **77**, 3865 (1996),.
- [23] P. Giannozzi, S. Baroni, N. Bonini, M. Calandra, R. Car, C. Cavazzoni, D. Ceresoli, G. L. Chiarotti, M. Cococcioni, I. Dabo, A. Dal Corso, S. de Gironcoli, S. Fabris, G. Fratesi, R. Gebauer, U. Gerstmann, C. Gougoussis, A. Kokalj, M. Lazzeri, L. Martin-Samos, N. Marzari, F. Mauri, R. Mazzarello, S. Paolini, A. Pasquarello, L. Paulatto, C. Sbraccia, S. Scandolo, G. Sclauzero, A. P. Seitsonen, A. Smogunov, P. Umari, and R. M. Wentzcovitch, *J. Phys. Condens. Matter* **21**, 395502 (2009).
- [24] G. Kresse and J. Furthmüller, *Phys. Rev. B* **54**, 11169 (1996).
- [25] M. Fuchs and M. Scheffler, *Comput. Phys. Commun.* **119**, 67 (1999).
- [26] D. R. Hamann, *Phys. Rev. B* **88**, 85117 (2013).
- [27] S. Poncé, E. R. Margine, C. Verdi, and F. Giustino, *Comput. Phys. Commun.* **209**, 116 (2016),.
- [28] A. A. Mostofi, J. R. Yates, Y.-S. Lee, I. Souza, D. Vanderbilt, and N. Marzari, *Comput. Phys. Commun.* **178**, 685 (2008).
- [29] E. R. Margine and F. Giustino, *Phys. Rev. B* **87**, 024505 (2013),.
- [30] Furuseth, S., K. Selte, and A. Kjekshus, *Acta Chemica Scandinavica* **19**, 257 (1965).
- [31] Supplemental Materials.
- [32] T. Thonhauser, V. R. Cooper, S. Li, A. Puzder, P. Hyldgaard, and D. C. Langreth, *Phys. Rev. B* **76**, 125112 (2007).
- [33] R. Sabatini, E. Küçükbenli, B. Kolb, T. Thonhauser, and S. De Gironcoli, *J. Phys. Condens. Matter* **24**, 424209 (2012).
- [34] I. Hamada, *Phys. Rev. B* **89**, 121103 (2014).
- [35] The optimized structure parameters of bulk PtTe₂ using the FHI98 (without vdW), which is a type of norm-conserving pseudopotential, are in nice agreement with experiment (see Table S1 [31]). Therefore, it is the best choice to using the FHI98 for all the calculations. However, we did not find the fully relativistic version of the FHI98, so that the SOC effect cannot be taken into account. Therefore, we turn to the ONCV pseudopotential, another type of norm-conserving pseudopotential, which has both the versions, so that the calculations with and without SOC can be performed, and the comparison of the results with and without SOC can be made. Therefore, we report the results of the ONCV (Figs. 2, 3 and 4) in the main text. Regarding the vdW correction, we find that the structure parameters optimized using ONCV with and without vdW are both reasonable and the former ones are closer to experiment (Table S1 [31]). On the other hand, we find that the density functional perturbation theory calculations are hard to converge when the vdW is included in the phonon calculations for the Pt₂Te₄ and RbPt₂Te₄. Therefore, the calculations of phonons, electron-phonon coupling and superconducting properties are using ONCV without vdW in the main text. We also examined the electronic struc-

- tures computed using the ONCV with and without vdW and found that the vdW correlation has little influence on the electronic structure of RbPt_2Te_4 , especially for the DOS at Fermi energy (Sec. 1 [31]). Furthermore, we also find the consistent results of superconducting T_c of RbPt_2Te_4 using the ONCV (11 K, Fig. S13[31]) and FHI98 (11.5 K, Fig. S11[31]) without vdW and SOC. Therefore, we believe that the results obtained using ONCV without vdW correction, which we report in the main text, are reliable. It should also be mentioned that for more efficient calculations of the systems containing large numbers of atoms and electrons, we adopt projector augmented wave pseudopotentials with an energy truncation of 29.4 Rydberg, in cooperation with vdW correction, for the *ab initio* molecular dynamic simulations of RbPt_2Te_4 using a $5 \times 5 \times 1$ supercell (see Sec. S3 [31]), and for determining the convex hull of $\text{Rb}_x(\text{Pt}_2\text{Te}_4)_{1-x}$ in a $3 \times 3 \times 1$ supercell [see Fig. 1(b)]. This type of pseudopotential also yields reasonable structure parameters as shown in Table S1 [31].
- [36] K. Selte and A. Kjekshus, *Acta chem. scand.* **18**, 697 (1964).
- [37] F. Zheng, C. Cai, S. Ge, X. Zhang, X. Liu, H. Lu, Y. Zhang, J. Qiu, T. Taniguchi, K. Watanabe, S. Jia, J. Qi, J.-H. Chen, D. Sun, and J. Feng, *Adv. Mater.* **28**, 4845 (2016).
- [38] Peacock, M. A., Thompson, R. M., *American Mineralogist*, **31**, 204 (1946).
- [39] K. Kim, S. Kim, J. S. Kim, H. Kim, J. H. Park, and B. I. Min, *Phys. Rev. B* **97**, 165102 (2018).
- [40] M. P. Allen and D. J. Tildesley, *Computer simulation of liquids* (Oxford university press, 1989).
- [41] F. Giustino, *Rev. Mod. Phys.* **89**, 015003 (2017),.
- [42] W. L. McMillan, *Phys. Rev.* **167**, 331 (1968).
- [43] P. B. Allen and R. C. Dynes, *Phys. Rev. B* **12**, 905 (1975).
- [44] K. H. Bennemann and J. W. Garland, in *AIP Conf. Proc.*, Vol. 4 (AIP, 1972) pp. 103–137.
- [45] H. J. Choi, D. Roundy, H. Sun, M. L. Cohen, and S. G. Louie, *Nature* **418**, 758 (2002).
- [46] A. Sanna, S. Pittalis, J. K. Dewhurst, M. Monni, S. Sharma, G. Umrigar, S. Massidda, and E. K. Gross, *Phys. Rev. B* **85**, 184514 (2012).
- [47] E. Sajadi, T. Palomaki, Z. Fei, W. Zhao, P. Bement, C. Olsen, S. Luescher, X. Xu, J. A. Folk, and D. H. Cobden, *Science* **362**, 922 (2018).
- [48] X. Fan, H. Chen, J. Deng, X. Sun, L. Zhao, L. Chen, S. Jin, G. Wang, and X. Chen, *Inorg. Chem.* **58**, 7564 (2019).
- [49] Y. Nakata, K. Sugawara, A. Chainani, K. Yamauchi, K. Nakayama, S. Souma, P.-Y. Chuang, C.-M. Cheng, T. Oguchi, and K. Ueno, *Phys. Rev. Mater.* **3**, 71001 (2019).
- [50] M. Bianchi, R. C. Hatch, Z. Li, P. Hofmann, F. Song, J. Mi, B. B. Iversen, Z. M. Abd El-Fattah, P. Löptien, L. Zhou, A. A. Khajetoorians, J. Wiebe, R. Wiesendanger, and J. W. Wells, *ACS Nano* **6**, 7009 (2012).